

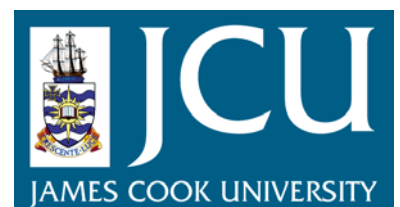
# JCU ePrints

This file is part of the following reference:

**Mantovanelli, Alessandra (2005) *A new approach for measuring in situ the concentration and settling velocity of suspended cohesive sediment*. PhD thesis, James Cook University.**

Access to this file is available from:

<http://eprints.jcu.edu.au/5326>



**A New Approach for Measuring *in situ* the  
Concentration and Settling Velocity of Suspended  
Cohesive Sediment**

Thesis submitted by  
**Alessandra Mantovanelli** (MSc) UFPR-Brazil  
in March 2005

for the Degree of Philosophy  
in the School of Mathematical and Physical Sciences  
James Cook University

## **Statement of access**

I, Alessandra Mantovanelli, the author of this thesis, understand that James Cook University will make it available for use within the University Library and allow access to user in approved libraries. All users consulting this thesis must sign the following statement.

In consulting this thesis I agree not to copy or closely paraphrase it in whole or in part without the consent of the author; and to make proper written acknowledgment for any assistance that I have obtained from it.

Beyond this, I do not wish to place any restrictions on access to the thesis.

---

Alessandra Mantovanelli

---

data

## **Statement of sources**

I declare that this thesis is my own work and has been submitted in any form for another degree or diploma at any university or other institution of tertiary education. Information derived from published or unpublished work of others has been acknowledged in the text and a list of references provided.

---

Alessandra Mantovanelli

---

data

## Acknowledgements

I wish to acknowledge Lance Bode (Department of Mathematics and Physics, James Cook University) for his supervision and support on this study and Peter Ridd (Department of Mathematics and Physics, James Cook University) for his supervision, friendship and support on this work and for giving me the opportunity of learning and developing something new.

I thank all the people who contributed in some aspect to this work and all staff of the Mathematics and Physics Department. My special thanks to Mal Heron for lending me a pressure sensor and helping me to use it, to Arnstein Prytz for his support on computer and data analysis, to Zachary Burrell for solving many of my computer crashes, to Russell Jaycock, Dee-Ann Belz, Marie Kirkham and Pauline Birrell for their technical assistance and kindness, to Raymond Casey for designing and building the electronic circuits used in the SEDVEL instrument and to Peter Smith for helping designing and manufacturing the SEDVEL. I would like to thank very much Jeffrey Cavanagh for his friendship and for having contributed a lot designing and building the SEDVEL instrument, finding always a creative and fast solution to improve it. Many thanks to James Whinney, Jonathan Bathgate, Adi Susilo, Severine Thomas, Thomas Stieglitz, Mariana Nahjas and Miguel Barbosa for their assistance in the field trips, data processing and friendship.

I also thank Michael Ridd (Department of Chemistry, James Cook University) for allowing me to use his laboratory facilities and Raphael Wüst (Department of Geology, James Cook University) for provision of some sediment density data used in this thesis. I acknowledge the staff of the Analytical Center and the Australian Center of Tropical Freshwater Research for allowing me to use their facilities to analyze some water samples and for their assistance on it, particularly John Faithful, Joanne Knott, Vivien McConnell, Sarah Thornton, Jenny-Lee Cook, Gordon Warria and Elvy Grigolato.

I acknowledge Jim Waldron from the Environmental Protection Agency (EPA) for making available the wave data of the Townsville Buoy and the Bureau of Meteorology for provision of the meteorological data recorded at the Townsville Airport.

I acknowledge the receipt of a scholarship to support this study from the Conselho Nacional de Desenvolvimento Científico e Tecnológico (CNPq, Brazil) and the Doctoral Merit Research Scheme (DRS) of James Cook University for its financial support.

I will always be grateful to the Ridd's families for their support and friendship during these years in Australia. Peter, Cheryl, Emma, James, Michael, Sue, Sarah and John, I thank you very much. Severine Thomas and Thomas Stieglitz thank you for your help, friendship and all pleasant moments we spent together. Sara, Leonardo, Laura and Paulo Busilacchi your friendship meant a lot.

Special thank for my family Lucia, Ricardo, Anaryá for their encouragement and love.

Very special thank to Eduardo for giving many insights for solving countless problems found during the instrument development and for his support throughout this work. Eduardo, Giovanni and Bruno thank you for your love, you have brought lots of inspiration and happiness to my life.

## Abstract

The settling velocity of suspended particulate matter (SPM) is a key parameter controlling deposition processes and its accurate determination has been regarded as a top priority in improving numerical models of cohesive sediment transport. Because SPM occurs predominantly as aggregates of organic and inorganic particles in cohesive coastal systems, an *in situ* quantification of settling velocity is essential. The available techniques to measure the settling velocity of aggregates in the field include: Owen tubes and similar, settling columns equipped with optical sensors, laser systems or video cameras as well as acoustics and holographic systems. None of these techniques is able to directly measure the mass-concentration of SPM or its settling velocity mass distribution *in situ*.

In this work, a new instrument (SEDVEL – Sedimentation Velocity) was developed to directly and automatically measure SPM mass of cohesive sediments *in situ*, from which the mass/concentration distribution of settling velocities can be determined. This instrument consists of an underwater balance (resolution of 0.01 g) placed inside a settling tube, which directly measures the variation in time of the immersed weight of particulate matter (*PM*) as it settles on a plate located at the tube bottom under quiescent conditions. SEDVEL operates underwater and automatically withdraws water samples — deployment periods of a few days. The design of SEDVEL and its components are described as well as the procedure adopted in its calibration and data analysis. Results of the assessment of the instrument performance in the laboratory and in the field are analysed.

SEDVEL presented consistent and reproducible results when tested in the laboratory. It was able to reproduce the initial particles concentrations ranging from 7 to 200 mg l<sup>-1</sup> ( $r^2 = 0.9$ ,  $p < 0.01$ ) in 13 laboratory experiments. Results also suggested that some particle reflocculation induced by the settling column can take place for concentrations higher than 50 mg l<sup>-1</sup>. Field trials, carried out in Cleveland Bay at Berth 11 (Townsville Harbour, Australia) and at the Pier (Strand Beach, Townsville, Australia), showed that SEDVEL reproduced the general tendency of the measured SPM concentrations in 42 cycles of measurement ( $r^2 = 0.65$ ,  $p < 0.01$ ).

At the Pier, settling velocities presented a main mode of relatively slow-settling particles/flocs within  $0.09 \leq W_s < 0.5 \text{ mm s}^{-1}$ , and usually a second mode of  $1.5 \leq W_s < 3.0 \text{ mm s}^{-1}$ . The settling dynamics at this location were mainly determined by erosion and deposition of sediment particles from and to the bottom close to the headland as well as by advection of offshore floc populations during the rising tide. At Berth 11, aggregates were composed mainly of microflocs of low-density and slow settling velocities ( $0.09 \leq W_s < 0.12 \text{ mm s}^{-1}$ ). The estimated mean density of flocs, 40% smaller than the density of inorganic particles, represented better the settling mode measured at this site.

SEDVEL constituted a novel idea for measuring settling velocities *in situ*, and therefore, a considerable amount of development, prototyping and testing was required. Compared with other automated instruments for measuring settling velocities *in situ*, SEDVEL has a relatively simple working principle, calibration and data analysis procedure. It is also unique in furnishing direct and automated *in situ* measurements of immersed mass and mass-concentration of SPM. The main problems associated with the current SEDVEL version are: zero position drifting among the different cycles of the measurement and from its initial set-up, possible floc break-up due to the pumping system used in the water replacement, errors associated with a non-homogeneous distribution of particles on the balance plate and with the definition of the zero position. A general assessment of SEDVEL potential limitations, and improvements to be achieved in future versions of the instrument, are described.

# Contents

Chapter 1. General introduction.....	1
1.1. Cohesive sediments in coastal systems .....	2
1.2. This work.....	5
1.2.1. Thesis outline.....	6
Chapter 2. Devices to measure settling velocities of cohesive sediment: a review of the <i>in situ</i> technology .....	8
2.1. Introduction .....	8
2.2. Direct measurements .....	10
2.2.1. Settling tubes manually operated (Owen-kind tubes) and their working principle.....	10
2.2.2. Advantages and constraints of the settling tubes.....	12
2.2.2. Settling columns equipped with automated in situ video cameras.....	15
2.2.2.1. Examples of the available video systems for settling velocity measurement.....	16
2.2.2.2. Advantages and constraints of the in situ video cameras .....	19
2.3. Indirect measurements.....	21
2.3.1. Settling columns equipped with optical instruments.....	21
2.3.1.1. Examples of <i>in situ</i> settling columns equipped with optical instruments ...	21
2.3.1.2. Advantages and constraints of settling columns equipped with optical instruments .....	23
2.3.2. Settling columns equipped with laser diffraction equipment .....	25
2.3.2.1. Advantages and constraints of settling columns equipped with a laser beam .....	27
2.4. Miscellaneous techniques .....	28

2.5. Non-intrusive measurements of settling velocity in a turbulent field .....	30
2.5.1. Direct holographic technique.....	30
2.5.2. Indirect acoustic methods .....	32
2.6. General assessment.....	35
2.7. Conclusions .....	39

### Chapter 3. SEDVEL: an underwater balance for measuring *in situ*

settling velocities and suspended sediment concentrations.....	41
3.1. Introduction .....	41
3.2. First ideas and prototypes .....	42
3.3. SEDVEL.....	52
3.3.1. General description and working principle .....	52
3.4. SEDVEL components.....	54
3.4.1. Displacement sensor .....	54
3.4.2. Magnetic spring .....	58
3.4.2.1. Magnetic field and induction.....	59
3.4.2.2. Magnetic spring balance set-up.....	61
3.4.3. Suspension system.....	64
3.4.4. Balance plate.....	66
3.4.5. Pan cleaning system and water replacement .....	69
3.4.6. Housing, data logger and controller circuits.....	71
3.4.7. SEDVEL operational procedure in the field.....	73
3.5. Balance Calibration and factors that affect its sensitivity .....	74
3.5.1. Verification of homogeneity of settled material.....	74
3.5.2. Balance calibration procedure .....	75
3.5.2.1. Calibration curves and balance sensitivity .....	75
3.5.2.2. Balance sensitivity for balance plates with different masses .....	79

3.5.3. Zero position changes.....	80
3.5.3.1. Influence of water density variations on the zero position.....	80
3.5.3.2. Salinity influence on the balance zero position.....	81
3.5.3.3. Bubbles.....	83
3.5.3.4. Magnetised sediment.....	83
3.6. Examples of SEDVEL measurements in the field.....	84
3.7. Advantages and constraints of SEDVEL.....	90
<b>Chapter 4. SEDVEL performance in the laboratory and <i>in situ</i>.....</b>	<b>96</b>
4.1. Introduction.....	96
4.2. Theory.....	100
4.2.1. Deposition of cohesive sediments.....	100
4.2.2. Odén theory of sedimentation applied to the analysis of settling tubes results.....	101
4.3. SEDVEL data analysis.....	104
4.3.1. Calculations of dry-mass and concentration of particulate matter (PM) from SEDVEL measurements.....	106
4.3.2. Aggregate density estimate.....	107
4.3.3. Calculations of deposition rates and settling velocities from SEDVEL measurements.....	109
4.4. Laboratory experiments.....	111
4.4.1. Experiments set-up.....	111
4.4.2. Experiments results.....	114
4.4.3. Reflocculation within settling columns and SEDVEL measurements in the laboratory.....	121
4.5. SEDVEL assessment <i>in situ</i> .....	125
4.5.1. Site of study.....	125

4.5.2. Field procedure and methods.....	127
4.5.3. SEDVEL estimates of the dry-mass concentrations versus measurements.....	128
4.5.4. SEDVEL estimates of mass distribution of settling velocity .....	134
4.5.4.1. Pier (Strand Beach).....	135
4.5.4.2. Environmental conditions at the Pier and the settling spectrum .....	144
4.5.4.3. Berth 11 .....	148
4.5.4.4. Mass-weighted average of settling velocities versus SPM concentrations.....	149
4.6. General assessment and conclusions .....	151
<b>Chapter 5. Summary and conclusion.....</b>	<b>155</b>
5.1. Suggestions for future SEDVEL improvements .....	162
<b>References.....</b>	<b>165</b>
<b>Appendix A: Basic concepts about magnetism .....</b>	<b>184</b>
<b>Appendix B: Relationship between the raw sensor output in Volts and in a arbitrary unit (data logger/controller output).....</b>	<b>185</b>
<b>Appendix C: Circuit diagram of the logical control of the slow rotation motor .....</b>	<b>186</b>
<b>Appendix D: Balance plate immersed weight calculation.....</b>	<b>187</b>
<b>Appendix E: Technical specification of the data logger and controller of SEDVEL instrument .....</b>	<b>188</b>
<b>Appendix F: Circuit diagram of the control of the pumps .....</b>	<b>189</b>
<b>Appendix G: Calibrations curves for the first SEDVEL version.....</b>	<b>190</b>

## List of Tables

Table 2.1. Summary of the main characteristics of *in situ* settling tubes. Pictures of the tubes were extracted from: <sup>1</sup> Fig. 2 of Eisma et al. (1997), <sup>2</sup> Fig. 3 of Eisma et al. (1997), <sup>3</sup> Fig. 1 of Jones and Jago (1996), <sup>4</sup> Fig. 5 of Eisma et al. (1997), <sup>5</sup> Fig. 1 of Cornelisse (1996), <sup>6</sup> Fig. 1 of Van Leussen (1996), <sup>7</sup> Fig. 1 of Puls and Kühl (1996) and <sup>8</sup> Fig. 11 of Bartz et al. (1985). Rows are numbered and their contents are as follow: 0 – Tube developer, 1 – Tubes dimensions for diameter and height ( $D \times H$ , cm), 2 – settling period (min), 3 – range of measurable SPM concentrations ( $\text{mg l}^{-1}$ ), 4 – range of measurable settling velocities ( $\text{mm s}^{-1}$ ), 5 – thermal insulation system when present, 6 – sampling position, 7 – sampling set-up, 8 – withdrawal system and sample volume (ml, unless otherwise specified), 9 – closure system, 10 – particularities of each tube and 11 – some references to obtain more information about tube description and field applications..... 13

Table 4.1. Resume of experimental conditions, including the average temperature and salinity, kind of particle used and the initial concentration ( $IC$ ,  $\text{mg l}^{-1}$ )..... 111

Table 4.2: Resume of the water density, initial dry-concentration ( $IC$ ), dry concentration estimated from SEDVEL measurements ( $\text{pan}$ ), the ratio between these two dry concentrations ( $\text{pan}/IC$ ), wet concentrations calculated based on the measured immersed masses, and the averaged settling velocity ( $\langle w_s \rangle$ , see Equation 4.18) calculated using time intervals of 20 ( $\Delta t = 20$  s) and 5 s ( $\Delta t = 5$  s) and the ratio between them, i.e.  $\langle w_s \rangle_{(5s)} / \langle w_s \rangle_{(20s)}$  ..... 117

## List of Figures

- Figure 1.1. Cyclical cohesive sediment transport (modified from Hamm and Migniot, 1994). 2
- Figure 2.1: (a) Typical Odén curve showing the temporal mass accumulation on the bottom of the settling tube for a SPM sample composed of 4 hypothetical discrete particles sizes ( $d_1 > d_2 > d_3 > d_4$ ). All particles are in suspension at  $t = t_0$ . When  $t = t_1$  all particles  $d_1$  plus some  $d_2$  and  $d_3$  particles have settled out of the suspension, and then successively as indicated by the circumferences on the picture; (b) Representation of the Odén curve in terms of percentage of material left in suspension. Figures adapted from Subcommittee on Sedimentation (1953). ..... 12
- Figure 2.2: Examples of underwater *in situ* video camera devices (a) schematic representation of VIS (Video *in situ*) (right) and an example of floating measurements of settling velocity in the EMS estuary during a tidal cycle (left) (modified from Fig. 1 and Fig. 3e of Van Leussen and Cornelisse, 1996) (b) Side (left) and top (right) views of a compact benthic video system with a honeycomb baffle (as presented in Fig. 1 of Sternberg et al., 1996). ..... 18
- Figure 2.3: (a) Remote optical settling *box* with pivoting doors and a sketch of a typical transmissometer output showing an increase in the transmissivity with time (modified from Fig. 2 and Fig. 3 of Hill et al., 1994), (b) schematic diagram of the *in situ* settling velocity box equipped with four miniature OBS sensors (MOBS) and example of the raw data showing the decaying of the backscatter signal with time at the four MOBS located at 2.5, 5.0, 10.0 and 20.0 cm below the top lid (modified from Fig. 1a and Fig. 4 of Murray et al., 1996). ..... 23

Figure 2.4: (a) Configuration of the laser particle sizer instrument (LISST-100) (b) and the LISST-ST settling column (Sequoia Scientific, Inc., Application note L002, Application note L007, <a href="http://www.sequoiasci.com">www.sequoiasci.com</a> ).	25
Figure 2.5: Diagram of the holographic array composed of a laser light that is spatially filtered and collimated, a remote sample volume and a CCD camera or holographic film connected to a computer and video monitor (modified from Owen and Zozulya, 2000; Costello et al., 1989).	31
Figure 3.1: A basic measurement principle of a SHS balance ( <a href="http://www.balances.com">www.balances.com</a> ).	43
Figure 3.2: Operating principle of the magnetic suspension balance manufactured by Rubotherm ( <a href="http://www.rubotherm.de">www.rubotherm.de</a> ).	44
Figure 3.3: (a) Schematic representation of the first prototype components (right) and a photograph of the balance plate (left). When the top and bottom electrodes are in contact, current flows through the water and closes the circuit with the external cylinder; and (b) calibration curves of the first balance performed in a freshwater tank; the masses of the discs placed on the top of the pan, varying from 0.2 to 2.1 g, are indicated on the legend.	46
Figure 3.4: (a) Schematic representation of the second prototype arrangement (b) calibration curves for the second prototype (3 replicates shown) realized in a freshwater tank. Standard weights were placed in front of the pan on the top of the small magnet (the most sensitive position, see Section 3.4.4) and (c) top view of the pan.	47
Figure 3.5: (a) Flux densities (mT) measured 1.5 cm above the top of two coils of 800 and 890 turns for the serial and parallel connections; (b) relationship between the current and the supplied voltage for the serial and parallel configurations of the two coils; and (c) input current to these two coils and the respective weight lifted.	48

Figure 3.6: (a) Third prototype schematic representation (lateral view); and (b) calibrations curves made in air with the third prototype, relating the magnet displacement (mm) to the accumulated dry-mass (g)..... 50

Figure 3.7: Calibration curve relating the balance plate displacement (mm) as function of the accumulated effective immersed mass ( $M_{EL}$ , g) in a freshwater tank. The balance plate position was visually marked and measured with a millimetre scale; the standard weights were placed in front of the pan (the most sensitive position, see Section 3.4.4). ..... 51

Figure 3.8: (a) First SEDVEL version: photography of the balance plate (top view, left) and sensor case (side view, right); (b) schematic representation of the balance plate (top view); and (c) examples of calibration curves for the first SEDVEL version considering two starting zero positions (1.4 and 1.7 Volts)..... 52

Figure 3.9: Schematic representation of the main body of SEDVEL (a) side view and (b) top view (right) and a photograph of the whole instrument (left top) and the balance plate (left bottom). Data logger/controller and battery case are not shown in the drawings. Arrows in the top photograph indicate the water flow direction during water replacement and the numbers the main parts of SEDVEL, namely: (1) data logger, (2) settling tube, (3) sensor case and (4) battery case. .... 53

Figure 3.10: (a) Photograph of the DVRT sensor manufactured by MicroStrain Inc., showing the sensor coil encapsulated in a stainless steel case (on the right) and the circuit board (on the left), and (b) a detail of the PVC membrane covering DVRT sensor head..... 55

Figure 3.11: Schematic representation of the eddy current transducer sensor, which detects changes in the measuring system's coil impedance caused by varying the distance

between the sensor (coil) and the surface of a conductive material (target).  $Z_{\text{eff}}$  is the effective impedance (extracted from Welsby and Hitz, 1997).....56

Figure 3.12: Response of the DVRT sensor plus a 0.4 mm PVC membrane (Volts) as function of the distance (mm) between the conductive target and the sensor head. The raw sensor output from the controller and data logger is shown for comparison. A relationship between the raw sensor output furnished by the data logger/ controller unit and the DVRT response in volts is presented in Appendix B. ....57

Figure 3.13: Plot of the slope (first derivative) of the DVRT raw sensor output ( $S_R$ ) as a function of the distance ( $x$ ) ( $dS_R/dx$ , white squares), and the ratio between the first derivative at the distance “ $i$ ” and the maximum slope (black squares):  $(dy_i / dx_i) / (dy / dx)_{\text{max}}$ . The last ratio ranges between 0 and 1. These derivatives were calculated based on the values presented in Figure 3.12 for the calibration curve of a +8V input for the DVRT sensor. Derivation was performed in Curve Expert 1.38, which uses a central difference scheme with Richardson extrapolation to compute the derivatives (Hyams, 2001). ...58

Figure 3.14: (a) Lines of magnetization ( $M$ ), flux induction ( $B$ ) and magnetic field ( $H$ ) for an ideal bar magnet (as presented in Duffin, 1980, Fig. 12.14) and (b) a typical  $B$ - $H$  curve and its main characteristics represented by the points at which it intersects the  $B$  and  $H$  axes, where  $B_r$  is the residual induction correspondent to the maximum flux that the magnet produces under closed circuit conditions;  $H_c$  is the coercive force that corresponds to the point at which the magnet becomes demagnetized under the influence of an externally applied magnetic field; and  $+B_m$  is the maximum flux density and  $+H_m$  is the maximum m.m.f applied, i.e. the maximum energy product (Design Guide, 2000: Group Arnold, 2000).....60

Figure 3.15: (a) Photograph of the magnet motor and gear box located inside the sensor case and (b) test to choose the gear set reduction for the slow rotation motor, showing the time needed for to the pan come back to its initial position (without load) after adding standard accumulative masses. This time is dependent on the gearbox ratio that moves

the magnet up to counteract the weight placed on the pan. See legend on the figure for the adopted reductions of the motor speed. ....63

Figure 3.15: (a) Photograph of the magnet motor and gear box located inside the sensor case and (b) test to choose the gear set reduction for the slow rotation motor, showing the time needed for to the pan come back to its initial position (without load) after adding standard accumulative masses. This time is dependent on the gearbox ratio that moves the magnet up to counteract the weight placed on the pan. See legend for the adopted reductions of the motor speed.....63

Figure 3.16: (a) Relationship between the repulsive force ( $F_R$ , N) between the two attached small magnets ( $D = 1$  cm,  $L = 0.6$  cm) and a big magnet ( $D = 2.4$  cm,  $H = 0.9$  cm) as a function of the distance ( $d_a$ , cm) they were set up apart, described by  $d_a = (9.10 \cdot 0.20 + 0.64 \cdot F_R^{0.64}) / (0.20 + F_R^{0.64})$  with  $r^2 = 0.99$ ; (b) a plot of the slope (first derivative,  $d(d_a) / d(F_R)$ , N cm<sup>-1</sup>) of the curve shown in Figure 3.16a, relating the variation in distance ( $d_a$ , cm) with the variation in the repulsive force between two attached small magnets ( $D = 1$  cm,  $L = 0.6$  cm) and a big magnet ( $D = 2.4$  cm,  $H = 0.9$  cm). This derivation was performed in Curve Expert 1.38, which uses a central difference scheme with Richardson extrapolation to compute the derivatives (Hyams, 2001) and (c) variation of the flux density ( $B$ , mT) with distance (cm) for a big ( $D = 2.40$  cm,  $H = 0.90$  cm) and a small ( $D = 1.00$  cm,  $H = 0.15$  cm) neodymium magnets. ....64

Figure 3.17: (a) Schematic drawing showing the components of the suspension system used to hold the balance plate (b) Photograph showing the suspension system fitting to the tube wall and (c) a detail of the spring system. ....65

Figure 3.18: Zero position set-up (first 6 minutes) and monitoring during 20 minutes..... 66

Figure 3.19: Photograph of the lower side of the aluminium pan with the two small magnets glued to it with a layer of epoxy resin. The position of the centre of mass ( $CM$ ) is also shown.....67

Figure 3.20: (a) Schematic drawing of the balance plate showing the six test positions (P1 to P5) and the centre of mass ( $CM$ ), (b) graphic showing the raw sensor output when a

aluminium disc is placed at the different tests positions (one position at each time) and also the value for the centre of mass position ( $CM$ ) and the averaged value for positions P1 to P5 ( $\bar{x}$ ) and (c) percentage of the raw sensor response increase or decrease in relation to the centre of mass output ( $CM$ ), considering the averaged output at P1 and P2, the averaged output at P3 and P5 and the output registered at P4. ....68

Figure 3.21: (a) Schematic drawing of the system to clean the balance plate; the two auxiliary pumps are turned on and the top pump stays off; (b) schematic drawing of the system for water replacement; the top pump is turned on and the water enters through the four opening inlets. The arrows indicate if the pipe works as an inlet or outlet to the settling tube. .... 70

Figure 3.22: Detail of the one-way silicone valve in its opened (a) and closed (b) positions.71

Figure 3.23: (a) Calibration curve showing the response of the DVRT sensor every time a new standard weight disc is added on the pan centre of mass. The first five minutes are used to set up the zero position, which is again monitored at the end of calibration when all discs are removed from the top of the pan. Every sensor output increment corresponds to the addition of a new disc on the top of the previous one. Spikes correspond to the instants of time when the weights have been manipulated; (b) Calibration curve relating the effective immersed mass ( $M_{EI}$ , g) to the raw sensor response, performed with PVC and aluminium discs (see legend on the Figure) for the same pan configuration. Experiment was realized with freshwater at temperatures between 18.9 and 19.2°C and similar starting zero positions..... 75

Figure 3.24: Set of calibration curves for the second SEDVEL version (aluminium Pan 4) relating the effective immersed mass ( $M_{EI}$ , g) to the raw sensor output ( $S_R$ ) for different starting positions. Calibrations were performed at salinities between 36 and 37 and

temperatures between 24 and 25°C. The maximum sensor output is located around 2350 (off scale)..... 76

Figure 3.25: Calibration curves showing the effective immersed mass ( $M_{EI}$ , g) as function of the raw sensor output ( $S_R$ , arbitrary units). The rational function adopted to relate these parameters is shown on the Figure. .... 77

Figure 3.26: First derivative ( $dM_I / dR_s$ ) for calibrations curves starting at the different zero positions showed in the inlet, relating the incremental variation in the effective immersed mass ( $M_{EI}$ , g) with the variation in the raw sensor output ( $S_R$ ). Original functions were rational equations in the form presented in Figure 3.25. This derivation was performed in Curve Expert 1.38, which uses a central difference scheme with Richardson extrapolation to compute the derivatives (Hyams, 2001)..... 78

Figure 3.27: Different calibration curves produced by balance plates of different immersed weights. Where  $M_{EI}$ ,  $\rho_W$ ,  $ZP$  are the immersed weight of the pan, water density and the zero position, respectively for each one of the tested pans. .... 80

Figure 3.28: Changing of SEDVEL raw output ( $S_R$ ) as a function of salinity for the different starting zero positions indicated in the legend. .... 81

Figure 3.29: Changing of SEDVEL raw output ( $S_R$ ) as a function of water density for the different starting zero positions indicated in the legend..... 82

Figure 3.30: (a) Data series of 57 consecutive cycles of SEDVEL measurements at the Townsville Harbour, (b) a detail of the first ten cycles of measurement. Each cycle lasted one hour and pumps were on for 60 s. .... 85

Figure 3.31: Displacement of the zero position calibration due to bubbles accidentally introduced in the tube during its filling before the deployment. .... 87

Figure 3.32: Deployments of the SEDVEL instrument at the Strand Beach (Townsville, Australia) (a) of the first SEDVEL version with opened inlets and outlets, showing the effect of the water percolation; (b) of the first SEDVEL version with inlets and outlets fitted with one-way valves and without the auxiliary pumps, showing the effect of improper pan cleaning; (c) of the second SEDVEL version using a short pumping period, showing the pan readings saturation, and (d) of the second SEDVEL version, showing a proper pan cleaning between the different cycles of measurement and reading stabilization at the end of each cycle. ....88

Figure 4.1: Relationship between the median settling velocity and concentration in different environments (extracted from Eisma et al., 1997, Figure 16, pg: 36). ....98

Figure 4.2: (a) Schematic representation of the Odén curve graphic method of obtaining the partially settled mass fraction ( $M_{PS}(t)$ ) and the completely settled mass fraction ( $M_{CS}(t)$ ), and (b) the method of obtaining the *OB* segments and the mass completely settled in each size or settling velocity fraction (i.e.  $m_{CS1}, m_{CS2} \dots m_{CS5}$ ). Based on these masses, the frequency histogram can be established (as drawn under the graphic). ....103

Figure 4.3: Variation of the raw sensor output with time during a cycle of measurement. The moment that the all pumps have stopped and the chosen zero position (*ZP*) are indicated in the graphic. Data collected at Strand Beach on 21/09/04. ....104

Figure 4.4: An example of interpolation of two calibration curves to get a new curve starting at the sought zero position ( $ZP_O$ , solid line). The  $ZP_{HO}$  and  $ZP_{LO}$  are represented by black circles and white triangles, respectively. ....105

Figure 4.5: Variation in the effective immersed masses ( $M_{EI}$ , g) as a function of sedimentation time (open circle) and the adjusted MMF model to the measured values (blue line). The adjusted model corresponds to  $y = (a \cdot b + c \cdot x^d) / (b + x^d)$ , and  $r^2 = 0.99$ .106

Figure 4.6: Relationship between <i>PM</i> density and the organic matter content ( <i>OM</i> ) expressed by $M_{OM}/M_{PM}$ ratio (1.0 = 100 wt-%). .....	108
Figure 4.7: (a) Schematic representation of SEDVEL settling tube set-up for the laboratory experiments (b) photo of the balance plate covered by a thin layer of sediment. Three vials glued to the tube bottom are also shown.....	112
Figure 4.8: Grain size distribution expressed as percent of the volume concentration analysed in the laser particle sizer (Malvern Mastersizer) of (a) the natural sediment collected at the Townsville Harbour and (b) glass beads particles.....	115
Figure 4.9: Relationship between the estimated dry-concentration of <i>PM</i> based on the maximum masses measured on the pan and the initial reference concentration ( <i>IC</i> ). The adjusted equation, $r^2$ and p values are given in the inset. ....	116
Figure 4.10: (a) Experiments with natural sediment run in freshwater (Series <i>A</i> ) at different initial sediment concentrations ( $[IC]$ , $\text{mg l}^{-1}$ ) as indicated on the picture, (b) linear regression between the averaged dry-mass of sediment ( $\text{g cm}^{-2}$ ) collected inside the vials and the dry-mass of sediment settled on the pan ( $\text{g cm}^{-2}$ ), (c) experiments with sediment run in saltwater (Series <i>S</i> ) at different initial sediment concentrations ( $[IC]$ , $\text{mg l}^{-1}$ ) and (d) experiments with glass beads (Series <i>GB</i> ) run in saltwater at different initial sediment concentrations ( $[IC]$ , $\text{mg l}^{-1}$ ). Points represent the original data and the lines the curves fitted to them. ....	119
Figure 4.11: Percent of mass plotted against the minimum settling velocity in each settling class (a) for initial sediment concentrations less than $50 \text{ mg l}^{-1}$ for the experiments of Series <i>A</i> and <i>S</i> , (b) for concentrations above $50 \text{ mg l}^{-1}$ for the experiments of Series <i>A</i> and <i>S</i> and (c) for concentrations above $50 \text{ mg l}^{-1}$ for the experiments of Series <i>GB</i> .	120

Figure 4.12: (a) Power correlation between the initial concentration of sediment ( $IC$ ,  $\text{mg l}^{-1}$ ) and the  $\langle W_s \rangle$  ( $\text{mm s}^{-1}$ ) for the experiments of Series  $A$  and  $S$ , (b) power correlation between the initial concentration of sediment ( $IC$ ,  $\text{mg l}^{-1}$ ) and mass percent of flocs with  $0.5 \leq W_s < 1.0 \text{ mm s}^{-1}$  for the experiments of Series  $A$  and  $S$ , and (c) power correlation between the initial sediment concentration ( $IC$ ,  $\text{mg l}^{-1}$ ) and mass percent of flocs with  $2.0 \leq W_s < 3.0 \text{ mm s}^{-1}$  for the experiments of Series  $A$  and  $S$ . All correlations were performed at 0.5% level of significance, the equations,  $r^2$  and  $p$  values are given in the inlets. .... 123

Figure 4.13: (a) Cleveland Bay located in Townsville (Australia), showing a detail of the two sampling areas: Berth 11 at the Townsville Harbour (right) and the Pier at the Strand Beach (left) (top map) and a photo of the Pier at the Strand Beach (bottom). The blue star indicates the site where the instruments were deployed. .... 126

Figure 4.14: Relationship between the dry mass concentrations of SPM ( $C_{(PM)_{dry}}$ ,  $\text{mg l}^{-1}$ ) estimated from SEDVEL measurements and those measured from the water samples collected concomitantly *in situ*. The adjusted equation,  $r^2$  and  $p$  values are shown in the inlet. .... 129

Figure 4.15: Relationship between dry density ( $\text{g cm}^{-3}$ ) and organic matter content (1.0 = 100 wt-%) of over 1230 sediment and peat samples (+) from a lake system in Malaysia (Wüst, 2001). The regression curve fitted to the data is represented by the red line ( $0.72/(1-0.70 \cdot \exp(-2.84 \cdot OM))$ ,  $r^2 = 0.42$ ). Measurements of SPM density effectuated in this work were not include in the regression, but are presented in the figure (blue squares) for comparison. .... 132

Figure 4.16: Percentage of mass distribution in each settling class for the deployments at the Pier (Strand Beach) (left) and size distribution of SPM (right), determined by the laser

particle sizer in the laboratory. Deployment dates, the starting times and concentrations of SPM for each cycle of measurement are shown in the inlets. These cycles were measured during the neap tide..... 135

Figure 4.17: Percentage of mass distribution in each settling class for the deployments at the Pier (Strand Beach) (left) and size distribution of SPM (right), determined by the laser particle sizer in the laboratory. Deployment dates, the starting times and concentrations of SPM for each cycle of measurement are shown in the inlets. These cycles were measured during the spring tide..... 137

Figure 4.18: Variation during the day of the tidal range (*a*), wind speed (*b*) and direction (*c*), and the significative wave height measured at Cape Cleveland (EAP, *Hs*) (*d*). Variation during the period of monitoring of the minimum and maximum wave heights at the Pier (visual observations, *d*), the current intensity (*e*) and the concentration (SPM,  $\text{mg l}^{-1}$ ) and organic matter content (OM, %) of SPM (*f*) on 02/09/04 (neap tide). ..... 139

Figure 4.19: Variation during the day of the tidal range (*a*), wind speed (*b*) and direction (*c*), and the significative wave height measured at Cape Cleveland (EAP, *Hs*) (*d*). Variation during the period of monitoring of the minimum and maximum wave heights at the Pier (visual observations, *d*), the current intensity (*e*) and the concentration (SPM,  $\text{mg l}^{-1}$ ) and organic matter content (OM, %) of SPM (*f*) on 06/09/04 (neap tide). ..... 140

Figure 4.20: Variation during the day of the tidal range (*a*), wind speed (*b*) and direction (*c*), and the significative wave height measured at Cape Cleveland (EAP, *Hs*) (*d*). Variation during the period of monitoring of the minimum and maximum wave heights at the Pier (visual observations, *d*), the current intensity (*e*) and the concentration (SPM,  $\text{mg l}^{-1}$ ) and organic matter content (OM, %) of SPM (*f*) on 15/09/04 (spring tide). ..... 142

Figure 4.21: Variation during the day of the tidal range (*a*), wind speed (*b*) and direction (*c*), and the significant wave height measured at Cape Cleveland (EAP, *Hs*) (*d*). Variation during the period of monitoring of the minimum and maximum wave heights at the Pier (visual observations, *d*), the current intensity (*e*) and the concentration (SPM,  $\text{mg l}^{-1}$ ) and organic matter content (OM, %) of SPM (*f*) on 27/08/04 (spring tide)..... 143

Figure 4.22: Relationship between SPM concentrations ( $\text{mg l}^{-1}$ ) and organic matter percentage considering all measurements effectuated at the Pier during 2003 and 2004. .... 146

Figure 4.23: Photographs taken at the Pier for comparison of the water turbidity close to the rock headland at the sampling site and at end of the Pier and offshore waters at the low-water of two spring tides: the spring of 31/08/04 (top) and the spring 27/08/04 (bottom). .... 146

Figure 4.24: Percentage of mass distribution in each settling class for the Berth 11 deployments (upper graphics) and size distribution of SPM (lower graphics), determined by the laser particle sizer in the laboratory. Deployment dates, the starting times and concentrations of SPM for each cycle of measurement are shown in the inlets. .... 148